Perovskite $CsPbBr_3$ single-crystal detector operating at 10^{10} photons/s/mm^2 for ultra-high flux X-ray detection

Lei Pan[1§], Indra Raj Pandey[1,2§], Antonino Miceli[3*], Vladislav V. Klepov[1], Duck Young Chung[2], and Mercouri G. Kanatzidis[1,2,4*]

[1]*Department of Chemistry, Northwestern University, Evanston, IL 60208, USA*

[2]*Materials Science Division, Argonne National Laboratory, Lemont, IL 60439, USA*

[3]*X-ray Science Division, Argonne National Laboratory, Lemont, IL 60439, USA*

[4]*Department of Materials Science and Engineering, Northwestern University, Evanston, IL 60208, USA*

[§]equally contributed

*Correspondence to: m-kanatzidis@northwestern.edu, amiceli@anl.gov

Abstract

Semiconductors for detecting hard radiation are confronted with considerable problems when operating at high photon fluxes. We report a perovskite $CsPbBr_3$ single-crystal detector capable of operating at X-ray fluxes of up to 10^{10} photons/s/mm^2 with beam area $\leq$ 0.25 mm^2 at 58.61 keV for current-mode X-ray detection. The spectrometer-grade $CsPbBr_3$ detectors show a gamma-ray energy resolution of ~7.5% at 122 keV for ^{57}Co and dark current as low as 4.3 nA (0.5 nA/mm^2) at a reverse bias voltage of 200 V (118 V/mm). The detector was tested at X-ray energies of 8.2, 10, and 58.61 keV at a synchrotron light source under a reverse bias voltage of up to 1000 V (588 V/mm). Under a sufficiently high bias voltage and within several hundreds of seconds X-ray exposure, good photocurrent linearity (goodness of fit $R^2 > 0.99$) and reproducibility were obtained up to a flux of ~ 10^{10} photons/s/mm^2 at beam area 0.25 mm^2 with Lower Limit of Detection of ~10^5 photons/s/mm^2 and Charge Collection Efficiency of ~100% for 58.61 keV X-rays. Accordingly, wide application of $CsPbBr_3$ detectors in high-flux X-ray detection is anticipated.

Introduction

Detectors for hard X-ray detection and imaging with high and ultra-high photon fluxes (ϕ_p) are critical in various areas. Medical X-ray imaging requires $\phi_p > 10^7$ photons/s/mm^2 (abbreviated as p/s/mm^2)[1], while modern Computed Tomography (CT) system requires $\phi_p \sim 10^9$ p/s/mm^2. Synchrotron X-rays can produce ultra-high flux of $\phi_p > 10^{10}$ p/s/mm^2, which can enable scientific advancements in numerical fields (e.g., material characterization, biological imaging, battery studies, and many others)[2-5]. In comparison, a laboratory X-ray tube typically can produce $\phi_p \sim 10^4$ - 10^8 p/s/mm^2 [6], many orders of magnitude lower than synchrotron. Direct conversion semiconductor X-ray detectors operating at room temperature are favored over scintillator-based indirect conversion detectors because of their high detection efficiency and intrinsic spatial resolution[7,8]. Large synchrotron facilities need semiconductor hard X-ray detectors that can handle the wide range of energies involved and the enormous fluxes required for imaging or spectroscopy applications[5,9]. The high fluxes of the hard X-rays, however, pose significant challenges on the semiconductor detector. High-Z semiconductors are favored for a high detection efficiency, but material polarization has remained a major issue. Polarization occurs because of excessive space-charge buildup inside the semiconductor[10-12], which distorts the electric field and deteriorates detector performance.

Generally, material polarization can be classified as bias-induced or radiation-induced[13,14]. Ion migration is a known contributing factor to bias-induced polarization, which occurs in some TlBr detectors[15]. Deep defect levels can also lead to bias-induced polarization because of space charge buildup under the influence of bias voltage[12], which is a prominent problem in some Schottky-type CdTe detectors[11,16]. Radiation-induced polarization is due to the trapping of radiation-generated free charge carriers. It depends on X-ray flux, detector bias voltage, irradiation time, detector thickness, and temperature, according to theoretical and experimental investigation[10,17]. A CdTe detector was shown to suffer from significant radiation-induced polarization at a flux of $\sim 9\times10^{10}$ keV/s/mm^2 [18]. CdZnTe (CZT) detectors have also received lots of attention for high flux X-ray detection[19,20], but CZT detectors also exhibit various degrees of radiation-induced polarization depending on crystal quality[6,21] (**Supplementary Table 1**). The most recently developed high-flux CZT detectors can operate at $\phi_p \sim 10^8$ p/s/mm^2 for 120 kVp tungsten X-rays tested at photon counting mode [6,22]. Nevertheless, the high cost associated with material growth

problems (e.g., Te inclusions[23]) continues to limit the wide application of CZT. Other materials, such as mercuric iodide (HgI_2)[24] and gallium arsenide (GaAs)[25,26], have also been considered for X-ray detection but with limited success. Perovskites have recently emerged as promising next-generation semiconductor radiation detectors[1,27,28]. Perovskite thin films can be solution-processed for flat-panel X-ray imagers[29,30], and bulk single crystals (e.g., $CsPbBr_3$) can be grown from melt or solution for gamma-ray spectroscopy[31,32] and X-ray photon counting[33]. Despite various widely reported types of perovskite X-ray detectors[34], there have been no reports on performance under ultra-high X-ray fluxes (e.g., ϕ_p>10^8 p/s/mm^2). Such harsh high flux working conditions impose stringent requirements on perovskite crystal quality, materials stability, and device fabrication. These requirements include large perovskite single crystals with low defects and minimal ion migration. In contrast, many perovskites exhibit prominent ion migration problems[35-37].

Here, we report the performance of an all-inorganic perovskite $CsPbBr_3$ single-crystal detector under synchrotron X-ray radiation with ultra-high fluxes from 5.8×10^6 to 1.9×10^{12} p/s/mm^2 at beam area $\leq$ 0.25 mm^2 at X-ray energies of 8.2, 10, and 58.61 keV. $CsPbBr_3$ single-crystal ingots were grown by the Bridgman growth method, and high-quality spectrometer-grade crystals were selected and fabricated into detectors. The detectors had low and stable dark current, e.g., 4.3 nA (0.5 nA/mm^2) at a reverse voltage value (Vr) of 200 V (118 V/mm), which enables a superior ability to detect weak X-rays (i.e., a small Lower Limit of Detection) and stable detector operation up to at least Vr = 1000 V (588 V/mm). The excellent crystal quality and high reverse bias voltage allowed a high charge collection efficiency (CCE) of ~100%, leading to a measured X-ray detection Sensitivity (S) that approximates the theoretical value. Under a sufficiently high bias voltage and within several hundreds of seconds, a linear and reproducible photocurrent response was obtained within a broad dynamic range from ~ 10^6 to ~ 10^{10} photons/s/mm^2 at beam area 0.25 mm^2 for 58.61 keV X-ray. Besides, we further tested the performance of $CsPbBr_3$ detectors under ultra-high fluxes up to the limit of the synchrotron facility, which could be taken as a proxy to accelerated polarization testing that provides valuable clues to the detector's long-term stability under lower flux applications. Our investigation demonstrates the promising performance of $CsPbBr_3$ detector for high and ultra-high flux X-ray detection, which could lead to essential scientific advancements of medical and biological imaging and various synchrotron-based X-ray techniques.

Results and Discussions

Spectrometer-grade $CsPbBr_3$ single-crystal detectors

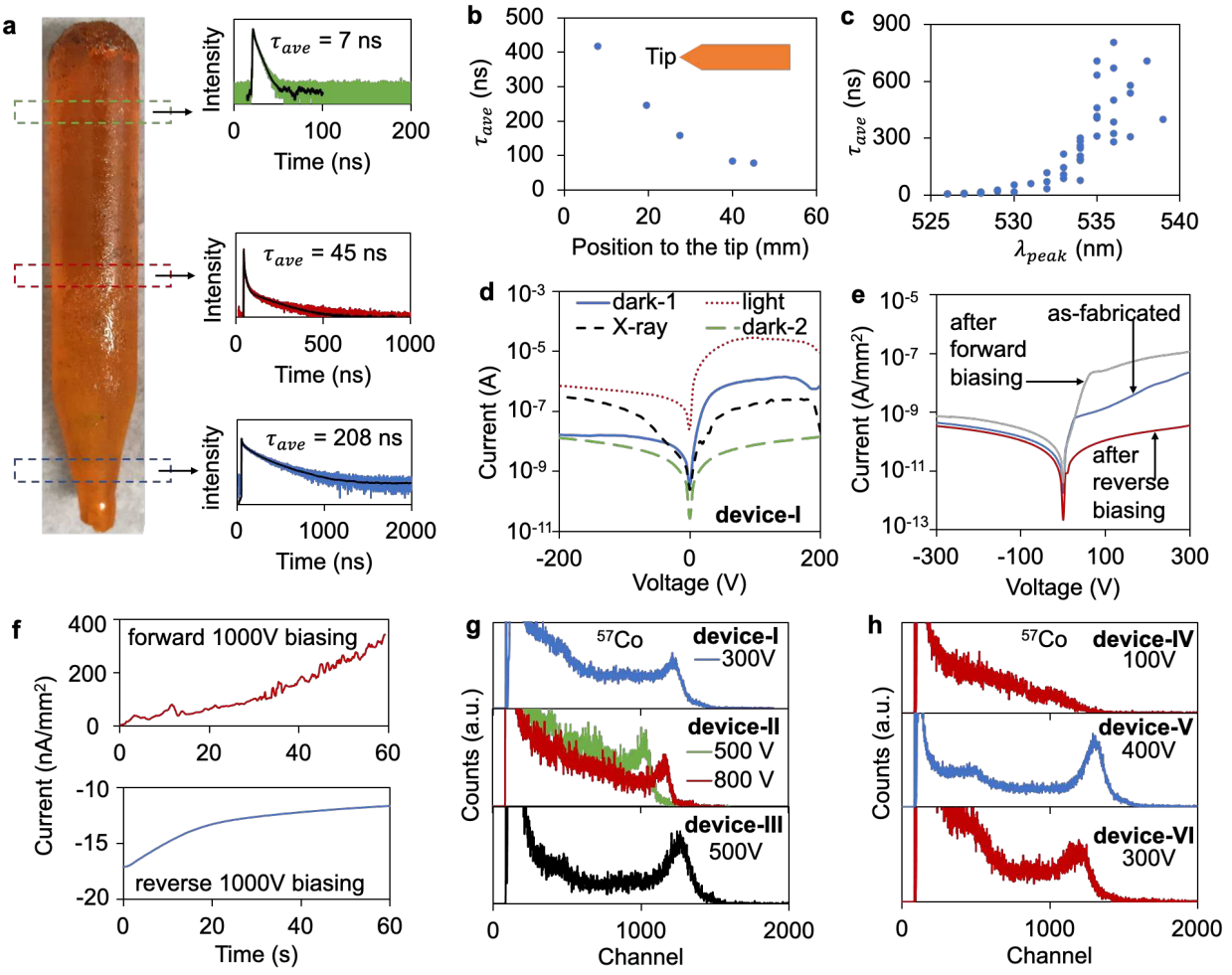

Fig. 1. $CsPbBr_3$ single-crystal detector quality screening. a. $CsPbBr_3$ ingot (diameter 16 mm) and Time-resolved PL spectrum of $CsPbBr_3$ crystals. τ_{ave} is average PL decay lifetime at the peak emission wavelength λ_{peak}. **b,** a typical relationship between τ_{ave} and crystal location of an $CsPbBr_3$ ingot. **c,** statistical data of τ_{ave} vs λ_{peak} obtained from many crystals of different ingots. **d.** I–V curves of device I. I–V curve testing sequence was "dark-1" (measured in dark before X-ray irradiation), "light" (under ambient room light), "X-ray" (under constant X-ray irradiation of 3.2×10^9 p/s/mm^2 at 8.2 keV), and "dark-2" (measured in dark right after X-ray irradiation). **e,** I-V curve of a $CsPbBr_3$ device measured after different biasing conditions. **f,** current as a function of time under constant biasing of forward and reverse 1000 V. **g, h.** ^{57}Co gamma-ray energy spectrum of as-fabricated $CsPbBr_3$ devices (shaping time: 10 μs; spectrum acquisition time: 300 s).

Given the aforementioned polarization mechanism [10,17], perovskite crystals with lower defects are expected to suffer less polarization and hence exhibit better device performance. We use photoluminescence (PL) spectroscopy to screen the $CsPbBr_3$ crystal quality. The as-grown

$CsPbBr_3$ ingot was cleaved at different positions, and PL of the freshly cleaved surface was measured (**Fig. 1a**). Time-resolved photoluminescence (TRPL) decay lifetime (τ_{ave}) has been associated with defect density in perovskite materials and are widely used as a proxy for crystal quality[38,39]. Theoretically, higher defect density means more free carriers would recombine through defect-assisted non-radiative (Shockley–Read–Hall) recombination, which results in weaker radiative recombination detected by TRPL and hence a shorter τ_{ave}. In fact, it has been frequently observed that lower defect density corresponds to a longer τ_{ave} in perovskite materials[40,41]. The $CsPbBr_3$ ingot has a PL lifetime τ_{ave} decreasing from the first-to-crystallize bottom tip to the last-to-crystallize top (**Fig. 1b**), which indicates a lower number of defects in the bottom. The $CsPbBr_3$ ingot quality gradient derives form varying impurity concentrations at different locations, which is a feature of the Bridgman growth method. Interestingly, we found that the steady-state PL emission peak wavelength λ_{peak} of the $CsPbBr_3$ crystal is correlated to the TRPL decay lifetime. Statistically, longer τ_{ave} usually corresponds to longer λ_{peak} (**Fig. 1c**). While the detailed mechanism behind the relationship between λ_{peak} and defects in $CsPbBr_3$ needs further investigation, we can grow and faithfully select high quality $CsPbBr_3$ crystals, represented by long τ_{ave} and λ_{peak} , for subsequent device fabrication and testing.

A high detector bias voltage is critical to mitigating radiation-induced polarization[10,17]. However, a high bias voltage could lead to large and unstable dark currents, which degrades the detector's ability to detect weak X-ray signals.[42] To maintain low dark current at a high bias voltage, we fabricated Schottky diode $CsPbBr_3$ detectors with gold and gallium indium eutectic alloy (denoted as GaIn) planar electrodes, i.e., Au/$CsPbBr_3$/GaIn. A Schottky/Ohmic contact is formed between the p-type $CsPbBr_3$ and the low/high work function metal GaIn/Au[43,44]. The direction of the electric field at reverse bias is from GaIn to $CsPbBr_3$. For gamma-ray and X-ray detection, the GaIn electrode side is irradiated. Given the limited penetration depth of X-rays (**Supplementary Fig.1**), holes contribute more to the induced signal. Because the hole mobility lifetime product, $\mu_h\tau_h$, exceeds the $\mu_e\tau_e$ of electrons in $CsPbBr_3$ (i.e., $\mu_h\tau_h \approx 1.3 \times 10^{-3}$ cm^2/V vs $\mu_e\tau_e \approx 8.8 \times 10^{-4}$ cm^2/V, as previously reported[32,45,46]), having holes contribute more to the signal can result in higher CCE (**Supplementary Fig.1** shows the setup). We fabricated and tested 6 devices made of $CsPbBr_3$ crystals with relatively long τ_{ave} and λ_{peak} from the high-quality parts of different ingots with same growth parameters described in our previous work[31,46]. (**Fig. 1a** shows the τ_{ave} of devices

I and II, **Supplementary Fig.2** shows the TRPL and PL emission spectra of the rest crystals, **Supplementary Fig.3** shows device pictures, **Table 1** shows crystal thickness).

Table 1. $CsPbBr_3$ detector parameters relevant to crystal and device quality.

Device	τ_{ave} (ns)	λ_{peak}(nm)	d (mm)	J_{dark} (nA/mm^2) at −200 V	ER (%) at 122 keV
I	208	536	1.9	1.5	~12.1
II	45	528	1.7	0.7	~7.5
III	140	540	1.7	0.5	~9.8
IV	19	533	1.7	3.5	-
V	538	537	1.7	3.6	~9.3
VI	50	535	1.7	11.6	~13.1

τ_{ave}: average PL decay lifetime; λ_{peak}: PL emission peak wavelength; d: detector thickness; J_{dark}: "dark-2" measured after irradiation; ER: energy resolution.

We measured the $CsPbBr_3$ detector I-V curve under different conditions: 1) in the dark, 2) under ambient room light, 3) under X-ray irradiation, 4) dark after detector irradiation. These measurements were performed sequentially in a single session. The voltage was swept from + 200 V to - 200 V and it took ~ 3 mins for each measurement (voltage step 5 V and ~ 2 s per current point). The dark I-V curve of the as-fabricated device and I-V under light illumination ("dark-1" and "light" in **Fig. 1d**) showed current-rectifying behavior due to the Schottky diode structure (**Supplementary Fig.4** depicts the I-V curves of other devices with similar behavior). Yet, we noticed some interesting results. As forward bias voltage ramps down from +200 V to 0V, the forward current first increases and then decreases. Besides, the I-V curve measured under X-ray irradiation and measured after X-ray irradiation in dark ("X-ray" and "dark-2" in **Fig. 1d**) became symmetric. The abnormal I-V behavior may be due to either ion migration or charge trapping. To confirm which factor dominates, we compared the dark I-V curves after different biasing conditions. As shown in **Fig. 1e**, the initial I-V of a freshly fabricated device showed a typical asymmetric diode behavior (voltage sweep from 0V to 300V, then from 0 V to -300V). During reverse 1000 V biasing for 1 min, the dark current kept decreasing and approached a steady value (**Fig. 1f**). After the reverse biasing, the I-V curve became symmetric with small leakage current at both reverse and forward bias directions (**Fig. 1e**). The $CsPbBr_3$ detector was then forward biased at 1000 V, and the initially small dark current gradually increased (**Fig. 1f**). Finally, the I-V curve returned to asymmetric diode behavior after forward biasing (**Fig. 1e**). The I-V curve change under different biasing conditions indicates ion migration in the $CsPbBr_3$ crystal, similar to results

reported elsewhere[47]. The continuous increase of current under repetitive forward biasing at a fixed X-ray flux further showed that charge trapping is not a major factor leading to the symmetric I-V curve (see **Supplementary Fig.4**). In the latter scenario, we would expect the forward current to decrease under X-ray irradiation. Ion migration occurs because of the presence of vacancy defects and can account for the fact that crystals obtained from different batches can behave differently as they may not contain identical numbers of defects or vacancies.

Regardless of the I-V curve change and ion migration, the $CsPbBr_3$ detectors work in reverse bias mode. By preconditioning the $CsPbBr_3$ detectors with reverse biasing, the dark current can reach a steady saturation value. A dark current, "dark-2" as low as 4.3 nA (0.5 nA/mm^2) at reverse voltage Vr = 200 V (118 V/mm), was achieved for the best device (device III). Different device fabrication aspects (e.g., electrode contact and wire connection) contribute to the variation in the dark current among all detectors (**Table 1**). High quality of both the $CsPbBr_3$ crystal and device fabrication is critical for excellent gamma-ray and X-ray detection performance. Five of the six devices can resolve the ^{57}Co 122 keV gamma-ray photopeak (Fig. 1g and Fig. 1h) with the best energy resolution of ~7.5% (Table 1), demonstrating that the ion migration is not fatal to the spectroscopy performance of the $CsPbBr_3$ detector.

Linear and reproducible current response up to 10^{10} p/s/mm^2

We first tested the $CsPbBr_3$ detector under synchrotron X-rays with ϕ_p = 10^8 – 10^9 p/s/mm^2 at energy (E_X) values of 8.2 and 10 keV. A high bias voltage is critical to reducing radiation-induced polarization[10,17], so we first tested detector responses at different bias voltages under a fixed photon flux. At $\phi_p = 3.2 \times 10^9$ p/s/mm^2 and E_X = 8.2 keV, the current response of device I is shown in **Fig. 2a**. The long current response time of several hundred seconds (i.e., the time from the start of current rising to stabilize) at low bias voltage (e.g. < 100 V) indicates significant radiation-induced polarization. As the X-ray generated free carriers continue to fill the traps in the crystal, more carriers are being collected, which leads to the slowly rising current. Contrarily, the response time is significantly reduced to several seconds or shorter at higher bias voltage, e.g., less than 1 s at 1000 V (588 V/mm) (see **Supplementary Fig.5** for the fast response at 1000 V), which means less radiation induced polarization. For comparison, we measured a spectrometer CZT detector whose response time is smaller than 1 s at 200 V (108 V/mm) (see **Supplementary Fig.6**), comparable to the $CsPbBr_3$ detector at high bias voltage. A short response time can enable a high frame rate,

important in imaging applications[48]. A photodiode's response speed may be limited by the carrier transit time or the RC time constant of the circuit[49]. We estimate the transit-time-limited 3dB cutoff frequency to be ~ 0.2 MHz for a $CsPbBr_3$ detector with thickness d = 1.7 mm at a bias voltage of 300 V, much smaller than the RC-limited 3dB cutoff frequency estimated to be ~ GHz order (see **Supplementary Info** for estimation). Therefore, the $CsPbBr_3$ detector response speed is typically limited by the charge carrier transit time instead of the RC effect. To increase the response speed, the bias voltage should be increased to reduce the carrier transit time. However, high bias voltage could result in large noise. Device surface passivation or guard ring structures may help to reduce noise.

Besides, a higher bias voltage can also benefit a higher CCE. As can be seen in **Fig. 2b**, the photocurrent density increases as a function of bias voltage and approaches saturation, which means CCE is increased at higher bias voltage (**Supplementary Fig.5** depicts raw current response at $\phi_p = 0.75 \times 10^9$ p/s/mm^2). Usually, the Hecht equation can be used to fit the photocurrent vs voltage data to estimate the charge carrier $\mu\tau$ product[32,45,46]. However, since significant polarization occurred at low bias voltage (e.g., < 100 V), the Hecht equation fitting would result in $\mu\tau$ value with error. Hence, we did not perform such fitting. Despite the advantage of reduced polarization, higher bias voltage could lead to large and unstable dark current (see **Supplementary Fig.5** and **Supplementary Fig.7** for the unstable dark current of some devices). As a rule of a thumb, the detector should be subjected to as high a bias voltage as possible without developing unstable dark current or breakdown. Following this as a selection rule, we chose a relatively high bias voltage of 300 V (158 V/mm) as the working voltage of device I and performed further testing. As shown in **Fig. 2c**, the detector has a stable dark current and fast response to different X-ray fluxes. The photocurrent density is linear at both E_X = 8.2 keV and E_X = 10 keV in flux range 10^8 – 10^9 p/s/mm^2 at beam area 1 mm^2 with goodness of fit $R^2 > 0.999$ (**Fig. 2d**) **(Supplementary Fig.5** shows the raw current response at E_X = 10 keV). The photocurrent is also linear against X-ray beam area at a fixed flux of $\phi_p = 2.98 \times 10^9$ p/s/mm^2 ($R^2 = 0.9984$) (**Fig. 2e**) (**Supplementary Fig.5** shows the raw current response). Similarly for device II, the photocurrent density J *vs*. ϕ_p at E_X = 8.2 keV showed good linearity at Vr > 300 V (**Fig. 2f**). At Vr < 300 V, the linearity is poor because of the radiation induced polarization (**Supplementary Fig. 8** shows the raw current response at different Vr and a fixed flux).

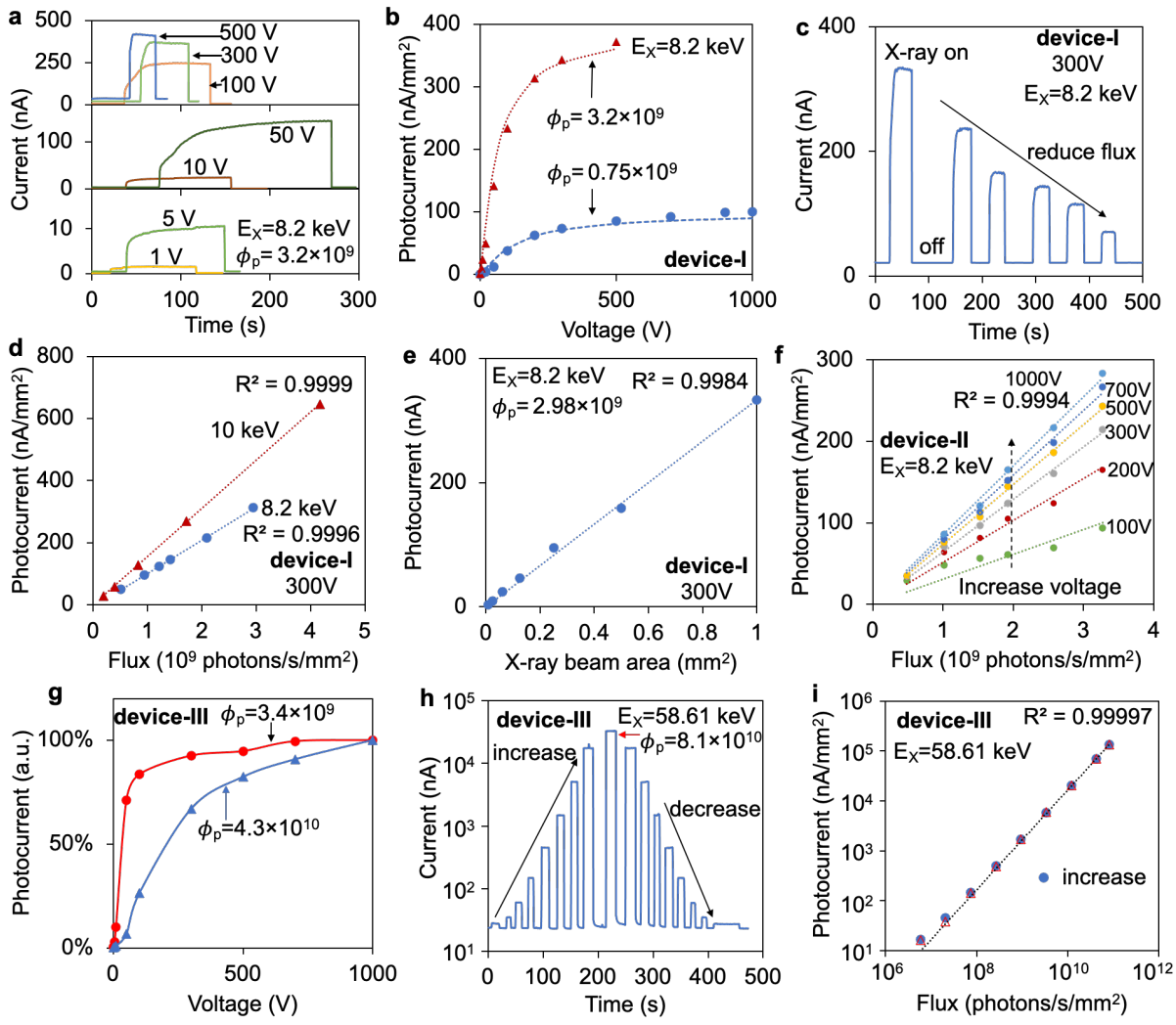

Fig. 2. Current response of $CsPbBr_3$ devices to synchrotron X-ray. E_X: X-ray energy; ϕ_p (p/s/mm^2): X-ray photon flux. R^2: goodness of fit for the linear fitting. **a.** Current response of device I under different reverse bias voltage (Vr) at a fixed flux (E_X = 8.2 keV, ϕ_p= 3.2 × 10^9 p/s/mm^2, A_{beam} = 1×1 mm^2). **b.** photocurrent density J vs. Vr of device I at different flux (E_X = 8.2 keV, A_{beam} = 1×1 mm^2). **c.** Device I current response to different ϕ_p in decreasing order (A_{beam}=1×1 mm^2). **d.** Device I J vs. ϕ_p at E_X = 8.2 and 10 keV (A_{beam} = 1×1 mm^2). **e.** Device I photocurrent vs. X-ray beam area A_{beam}. **f.** J vs. ϕ_p of device II at different Vr (A_{beam}=1×1 mm^2). **g.** Current response of device III to different Vr under fixed ϕ_p values (A_{beam} = 0.2×0.2 mm^2. Photocurrent normalized to that of 1000V to highlight the trend of current increasing). **h.** Current response of device III to different ϕ_p values (A_{beam} = 0.5×0.5 mm^2; Vr = 1000 V). **i.** Device III photocurrent density obtained during increasing and decreasing flux shown in **h**.

After testing under softer X-rays of 8.2 and 10 keV, we tested under 58.61 keV X-rays that have a larger penetration depth. A broader photon flux of ϕ_p= 5.8 × 10^6 to 8.1 × 10^{10} p/s/mm^2 were used. The current response at different applied Vr values under a fixed ϕ_p was first measured to determine working Vr values for different devices (see **Supplementary Fig.7**). The effect of bias

voltage on polarization was observed with the plot of photocurrent vs bias voltage for device III (**Fig.2g**). At a lower flux ϕ_p = 3.4 × 10^9 p/s/mm^2, the photocurrent quickly increases and approaches saturation. In comparison, at a higher flux ϕ_p= 4.3 × 10^{10} p/s/mm^2, the photocurrent was suppressed at a lower bias voltage region due to radiation-induced polarization. Different devices may exhibit different photocurrent saturation behavior due to different extents of polarization (see **Supplementary Fig.9** for photocurrent vs bias voltage for devices IV, V and VI).

Based on the bias voltage selection rule mentioned above, the optimal working Vr value was selected as 1000 V (588 V/mm) for device III and V, and 300 V (176 V/mm) for device IV and VI. For device III with Vr = 1000 V, ϕ_p first increased from 5.8 × 10^6 to 8.1 × 10^{10} p/s/mm^2 and then decreased back to 5.8 × 10^6 p/s/mm^2 with the same flux values (**Fig. 2h**). Stable dark and signal currents were obtained for all fluxes over several hundreds of seconds, indicating negligible radiation-induced polarization. Without polarization, the photocurrent obtained with increasing ϕ_p agrees with that obtained from decreasing ϕ_p (**Fig. 2i**), indicating a good reproducibility of the detector photocurrent at the same X-ray flux and a good linearity (R^2 = 0.99997). In addition, devices IV and V also showed good current linearity in the ϕ_p range 5.8 × 10^6 – 3.4 × 10^9 p/s/mm^2 (see **Supplementary Fig.10**). We note that the photocurrent magnitude may vary considerably between different devices due to the different device testing and polarization history. In summary, under sufficiently high bias voltage (e.g., 1000 V), the best-tested $CsPbBr_3$ detector (device III) can be operated at ϕ_p as high as 8.1 × 10^{10} p/s/mm^2 at E_X = 58.61 keV and beam area 0.25 mm^2 with good current stability, reproducibility, and linearity in a timescale of several hundreds of seconds. In comparison, a CdTe detector shows significant radiation-induced polarization at an energy flux of ~ 9×10^{10} keV/s/mm^2 [18], and the high-flux capable CZT detector can be operated at ~10^8 photons/s/mm^2 without noticeable polarization[6,22] (see **Supplementary Table 1** for comparison of $CsPbBr_3$ vs CdTe and CZT).

Sensitivity and Lower Limit of Detection (LLD) are important figures of merit of X-ray detectors[42]. Different from the polychromatic X-ray sensitivity (defined as $S = J/\dot{D_{air}}$, where J is the photocurrent density, and $\dot{D_{air}}$ is the X-ray dose rate in air), we calculate the sensitivity of monochromatic synchrotron X-rays by Equation (1), because the photon flux ϕ_p and energy E_X of synchrotron X-rays are readily known. Theoretically, the highest sensitivity, S_0, when CCE = 100% can be calculated using Equation (2) (**Supplementary Info** shows the derivation of S_0). Then, the

LLD can be calculated according to an established dark current method[42] using Equation (3), where A_{eff} is the effective area of current generation (i.e., the smaller area between X-ray beam and electrode), and $\sigma_{I_{dark}}$ is the standard deviation of the dark current. The sensitivity S and LLD for devices III – V at respective working bias voltage is shown in **Table 2**. The measured sensitivities approach the theoretical sensitivity of S_0 = 3 × 10^{-8} nC/keV (ε_{pair}= 5.3 eV for $CsPbBr_3$[46]) indicating that ~100% of the 58.61 keV photons were absorbed by the $CsPbBr_3$ crystal (i.e., negligible absorption by electrode), and CCE is ~100%. In addition, the sensitivity remains nearly constant within the linear dynamic range (The sensitivity is the slope of the linear fitting of photocurrent vs X-ray energy flux). Both sensitivity and dark current fluctuation influence the LLD, so LLD reflects the crystal and device fabrication quality. Device V has a much higher LLD due to its large dark current and fluctuation (see **Supplementary Fig.10**).

$$S\left(\frac{nC}{keV}\right) \equiv \frac{J\,(nA/mm^2)}{\phi_p\,(photons/s/mm^2)\cdot E_X(keV)}, \tag{1}$$

$$S_0\left(\frac{nC}{keV}\right) = \frac{1.6\times10^{-7}}{\varepsilon_{pair}}, \tag{2}$$

$$LLD(p/s/mm^2) = \frac{3.29\,\sigma_{I_{dark}}\,(nA)}{A_{eff}(mm^2)\cdot S\left(\frac{nC}{keV}\right)\cdot E_X(keV)}, \tag{3}$$

Table 2. Sensitivity S and LLD of devices III, IV, and V

device	Vr (V)	LLD (p/s/mm^2)	S (nC/keV)
III	1000	4 × 10^5	3.1 × 10^{-8}
IV	300	6 × 10^5	2.8 × 10^{-8}
V	1000	3 × 10^6	2.9 × 10^{-8}

A_{beam} = 0.2 × 0.2 mm^2 for devices IV; A_{beam} = 0.5 × 0.5 mm^2 for devices III and V; Because photocurrent is affected by device polarization history, S was calculated using a single point at 3.4 × 10^9 p/s/mm^2 before any polarization occurred at higher fluxes.

Accelerated polarization testing of $CsPbBr_3$ detector

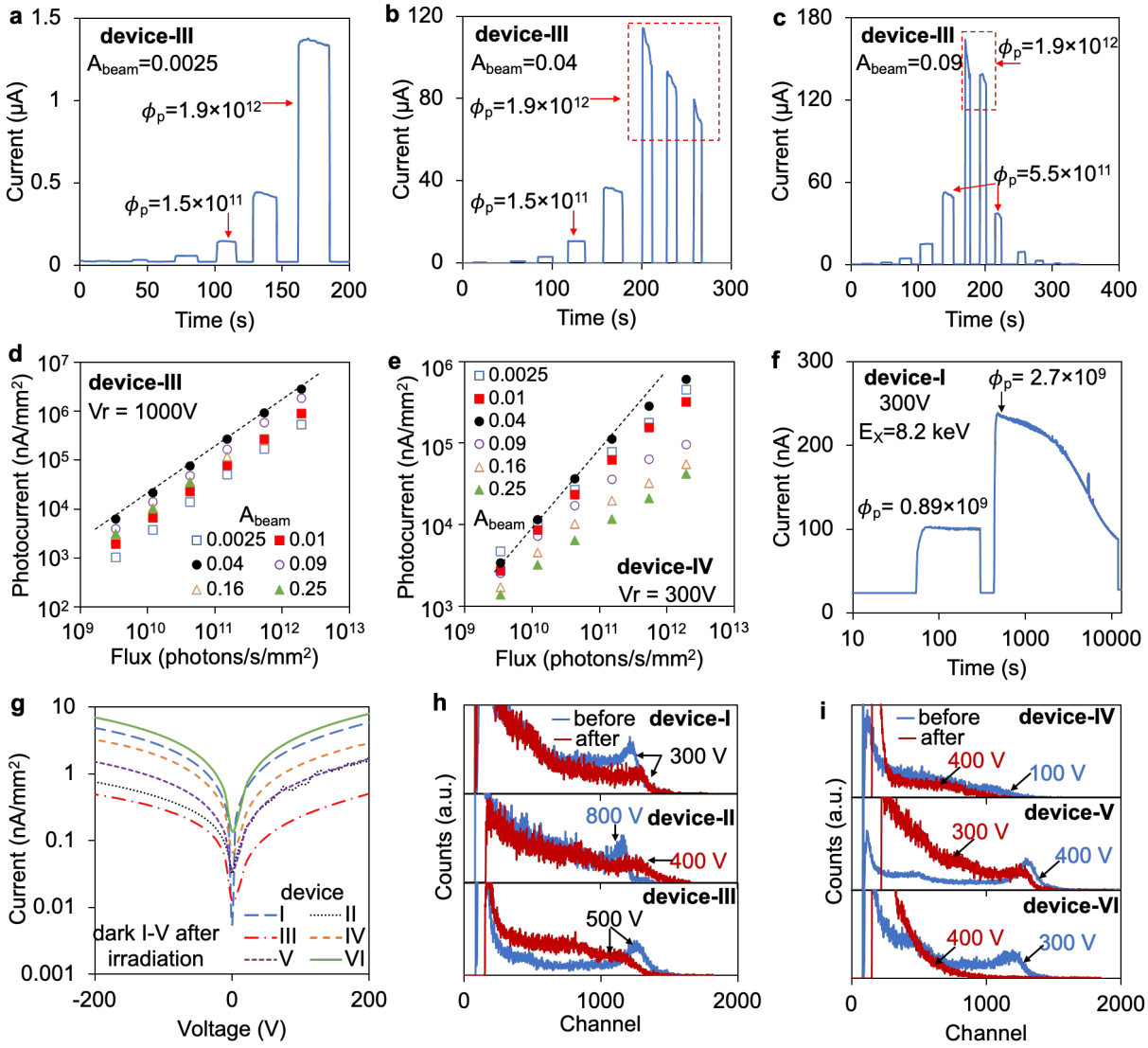

Fig. 3. Accelerated polarization testing of $CsPbBr_3$ detector. a, b, c. Current response of device III to different ϕ_p values with different X-ray beam area (Vr:1000 V; A_{beam} unit: mm^2). **d, e.** Photocurrent density J vs ϕ_p for device III (Vr = 1000 V) and device IV (Vr = 300 V) at different A_{beam} values. **f.** device I current response under continuous irradiation for several hours. A_{beam} = 1×1 mm^2. **g,** dark I-V curve of all devices after X-ray irradiation (voltage scan from +200 V to -200 V, voltage step 5 V, ~ 2 s per point). **h, i.** comparison of ^{57}Co gamma-ray energy spectrum of $CsPbBr_3$ detectors before and after synchrotron irradiation. Spectrum acquisition parameters: acquisition time 300 s, shaping time 10 μs.

So far, we have seen good linearity and reproducibility of the $CsPbBr_3$ detectors under a time scale of several hundred seconds. We further performed accelerated polarization testing of the $CsPbBr_3$ detector by increasing the X-ray flux or the irradiation time. Compared to the previous flux range of $\phi_p \sim 5.8 \times 10^6$ to 8.1×10^{10} p/s/mm^2, the devices were tested at a higher flux range of $\phi_p \sim 3.4 \times 10^9$ to 1.9×10^{12} p/s/mm^2 that is the flux limit of the synchrotron beamline. As shown in **Fig. 3a**

for device III, while current drifting is negligible at lower fluxes (e.g., $\phi_p < 1.5\times10^{11}$ p/s/mm^2), it decreases significantly above 1.5×10^{11} p/s/mm^2. When the dose is further increased by increasing the X-ray beam size from $A_{beam} = 0.05\times0.05$ mm^2 to $A_{beam} = 0.2\times0.2$ and 0.3×0.3 mm^2 (**Fig. 3b** and **Fig. 3c**), the current drifting became more prominent, which indicates that the polarization is area dependent. Additionally, under repeated tests at the same flux of $\phi_p = 1.9 \times 10^{12}$ p/s/mm^2 (**Fig. 3b** and **Fig. 3c**), the signal current could not recover its initial value (i.e., value before decreasing). The signal current follows the end value in the last test, indicating significant radiation-induced polarization. Once significant polarization occurred, even at the same lower flux (e.g., $\phi_p < 1.5 \times 10^{11}$ p/s/mm^2) where polarization is negligible, the signal current after significant polarization became smaller than its original value before polarization (**Fig. 3c**). This means that polarization degrades the reproducibility of the detector current. In contrast, good current reproducibility was obtained at lower flux values where no significant polarization occurred (**Fig. 2g**). At larger beam sizes of $A_{beam} = 0.4\times0.4$ and 0.5×0.5 mm^2, reducing the highest ϕ_p from 1.9×10^{12} to 1.5×10^{11} and 4.3×10^{10} p/s/mm^2, respectively, leads to better current reproducibility than that at ϕ_p=1.9×10^{12} p/s/mm^2 (**Supplementary Fig. 11** shows the raw current response). Despite the previous polarization at the flux limit of the synchrotron facility ϕ_p=1.9×10^{12} p/s/mm^2, subsequent testing with ϕ_p in a lower range of 5.8×10^6 – 4.3×10^{10} p/s/mm^2 shows good current reproducibility and linearity (**Supplementary Fig. 11**). Since the significant polarization at flux above certain level is detrimental to detector performance, it is important to understand the higher limit of flux under which the polarization is not a concern in several hundred seconds. However, as shown in **Fig. 3a,** the degree of polarization manifested by the current drifting became progressively prominent, so it is difficult to quantify the higher limit of flux precisely. Here, we try to find out a higher limit of photon flux by examining the current drifting (see **Supplementary Info** for details). The current drifting is negligible under ~ 20 s irradiation of flux of 8.1×10^{10} p/s/mm^2, 3.4×10^9 p/s/mm^2, and 1.2×10^{10} p/s/mm^2 at 58.61 keV, respectively, for device III, IV and V. These flux values may be taken as the higher limit of flux for respective devices.

Despite the current decreasing at higher flux due to polarization, we examined the linearity of photocurrent density J vs. ϕ_p with J calculated from the peak photocurrent before decreasing. As shown in **Fig. 3d**, good linearity was obtained for device III. However, practically, the detector should not be operated at $\phi_p > 1.5 \times 10^{11}$ p/s/mm^2 where significant current decreasing occurs due

to polarization. In comparison, device IV had photocurrent density deviated from linearity at flux $\phi_p > 1.5 \times 10^{11}$ p/s/mm^2 due to polarization (**Fig. 3e**). Increasing the bias voltage to 1000 V could not improve the linearity for device IV (**Supplementary Fig.12**). The worse performance of device IV than device III may be due to worse crystal quality (e.g., shorter τ_{ave}). Device V and VI also showed a photocurrent density deviation from linearity (**Supplementary Fig.12**). Ideally, the photocurrent density should be independent of the X-ray beam area. As shown in **Fig. 3d**, however, the fact that photocurrent density is different for different beam areas indicates that polarization occurred along the testing track, and the photocurrent density is affected by the testing sequence. Given the progressive behavior of polarization, we further tested the $CsPbBr_3$ detector under continuous irradiation for several hours at a low photon flux that polarization is not a concern in several hundred seconds. As shown in **Fig. 3f**, the decrease in the signal current of device I is negligible in several hundred seconds at a lower flux $\phi_p = 0.89 \times 10^9$ p/s/mm^2 (Vr = 300 V, E_X = 8.2 keV, A_{beam}=1 mm^2). However, at a higher flux of $\phi_p = 2.7 \times 10^9$ p/s/mm^2 and a longer time scale of several hours, the current shows significant drift, which suggests that the accumulated continuous irradiation plays a role in detector polarization. $CsPbBr_3$ device II, III and V exhibited similar current decreasing behavior in a time scale of several hours (see **Supplementary Fig.13**).

Finally, we measured the dark I-V curve and the ^{57}Co gamma-ray energy spectrum of the devices after testing under synchrotron X-ray. Since the devices were under reverse bias for several hours, the dark I-V curves remained symmetric with a small forward bias current (**Fig.3g**). The dark currents at reverse 200 V after synchrotron X-ray testing are comparable to that before testing (**Table 3**). The dark current change (several nA/mm^2 or less) is much smaller than the photocurrent produced by X-rays (10^1 - 10^5 nA/mm^2), and therefore, does not harm the device performance reproducibility. The energy spectrum of the detectors showed different degree of degradation due to detector polarization (**Fig. 3h, Fig. 3i)**. A polarized detector may recover after remaining under dark ambient conditions for several months, as observed in our previous work[33]. Active depolarization techniques, such as switching the bias voltage direction[18], infrared LED illumination[50], and heating, may be effective in accelerating $CsPbBr_3$ detector recovery, which needs further investigation.

Table 3. Comparison of device dark current at reverse 200 V before and after testing under synchrotron X-ray

	I	II	III	IV	V	VI
J_{dark} (nA/mm^2) - before	1.5	0.7	0.5	3.5	3.6	11.6
J_{dark} (nA/mm^2) - after	4.8	0.7	0.5	3.2	1.5	7

Conclusions

We developed efficient $CsPbBr_3$ crystal and device quality screening procedure with photoluminescence spectroscopy and I-V measurement and found out that the ion migration does not necessarily affect the performance of the $CsPbBr_3$ detectors. With the spectrometer-grade $CsPbBr_3$ detectors fabricated from high-quality crystals, a bias voltage of at least 1000 V (588 V/mm) can be applied, which is critical to reducing the polarization and hence enable a good detector photocurrent linearity and stability. Consequently, we demonstrated that the $CsPbBr_3$ detectors could operate at ultra-high X-ray fluxes of up to 10^{10} p/s/mm^2 with beam area 0.25 mm^2 at 58.61 keV with good photocurrent linearity, stability, and reproducibility over a timescale of several hundreds of seconds. The capability of the $CsPbBr_3$ detector operating in current mode under ultra-high flux without significant polarization could also benefit its performance in the pulse mode as photon-counting detector[33] because the underlying physics of polarization is the same for the current and pulse modes. Future work will focus on a) further improvement of crystal quality and the device fabrication process to further increase the bias voltage that can be applied and b) investigations of the dynamics and mechanisms of $CsPbBr_3$ polarization and its potential recovery.

Acknowledgments

This work has proceeded in part of a U.S. Department of Energy Basic Energy Sciences supported collaboration between ANL, SLAC, BNL and Cornell University to explore hi-Z detector materials. The study utilized the resources of the Advanced Photon Source (a U.S. DOE Office of Science user facility operated for the DOE Office of Science by Argonne National Laboratory) under Contract No. DE-AC02-06CH11357. This research was also supported in part by the Defense Threat Reduction Agency (DTRA) under the Interaction of Ionizing Radiation with the Matter University Research Alliance under contract number HDTRA1-20-2-0002. We

acknowledge the assistance of Leighanne Gallington, Tiffany Kinnibrugh, Uta Ruett, and Olaf Borkiewicz at the Advanced Photon Source at beamline 11-ID-B. We thank the entire DOE high-Z team at Argonne, Brookhaven, Cornell and SLAC for useful discussions.

Competing interests

Mercouri G. Kanatzidis and Duck Young Chung are cofounders of Actinia Inc, a company that applies perovskite materials to radiation detection.

Data availability

All data are available in the main text and Supplementary Information.

Methods

Crystal growth and device fabrication. The Bridgman method was employed to grow $CsPbBr_3$ single crystals. The growth process parameters and cooling schemes have been previously described in detail[31,46]. Ingots of $CsPbBr_3$ were cut into pieces of appropriate dimensions for detector fabrication. First, the surfaces of $CsPbBr_3$ crystals were finely polished using sandpaper and then cleaned with toluene. A gold electrode, approximately 100-nm thick, was thermally evaporated onto the crystal surface. Then, a liquid GaIn electrode was brushed onto the crystal surface. We note that the thickness of the GaIn electrode could be non-uniform and may be in the range from several hundred nm to several hundred μm. The thick GaIn electrode could absorb a significant portion of 8.2 keV and 10 keV X-rays (see **Supplementary Info** for an example calculation) and results in different photocurrent magnitude for different devices due to the non-uniform thickness. A copper wire connected the electrodes to the outer circuit, and crystals with a finished electrode and wire connection were placed on a glass holder encapsulated in paraffin wax.

Detector testing setup under synchrotron X-ray. Detector testing under synchrotron X-rays was performed at the Advanced Photon Source, Argonne National Laboratory. Measurements were performed at beamlines 1-BM-B and 11-ID-B, which provide 8.2 and 10-keV, and 58.61-keV X-rays, respectively. The experimental setup is illustrated in **Supplementary Fig. 14.** An ion chamber that measures the X-ray intensity directly out of the shutter, a set of adjustable slits that controls the beam area, and a $CsPbBr_3$ detector that is mounted on an X–Y–Z stage are located in sequence downstream of the beam shutter. The detector was first aligned with the X-ray beam using a laser-alignment tool. Then at a low X-ray flux, the detector position was fine-tuned to find

the position that generates a maximum current. As shown in **Supplementary Fig. 15,** because the GaIn electrode could be very thick at the center region (e.g., several hundred μm), the maximum current is usually produced when the X-ray beam irradiates the edge area. The X-ray flux at beamline 1-BM-B was modified by detuning the second crystal monochromator of the beamline facility, and the X-ray flux at beamline 11-ID-B was varied using a set of attenuators. A calibrated Si PIN diode was inserted into the X-ray beam path to measure the flux received by the $CsPbBr_3$ detector (**Supplementary Table 2** summarizes the flux calibration for beamline 11-ID-B).

Photoluminescence and electrical characterization. An FS5 spectrofluorometer (Edinburgh Instruments) was used to measure the time-resolved PL spectra and PL emission spectra at room temperature. The exciting wavelength for PL measurement is 375 nm generated by a laser. A Keithley 6517 B electrometer was employed to apply bias voltage to the $CsPbBr_3$ detector and measure current.

Gamma energy spectrum acquisition. The gamma spectroscopy system used for gamma energy spectrum acquisition included an eV-550 preamplifier, a 572A shaping amplifier (ORTEC), and a 927 multi-channel analyzer (ORTEC). The energy resolution of the photopeak was calculated as the full width at half maximum divided by the peak channel number. A shaping time of 10 μs is used. Given hole mobility of ~52 $cm^2/V/s$ and thickness d=1.7 mm, at a bias voltage of 300 V, the charge carrier drift time $\tau_{tr} = d^2/(\mu V)$ is estimated to be ~1.85 μs. Since the shaping time is larger than τ_{tr}, the ballistic deficit is not a concern affecting the energy spectroscopy performance. Ideally, the same bias voltage should be used for detector testing and performance comparison. However, the detector noise could change after heavy irradiation. The highest bias voltage without excessive noise was used for energy spectrum acquisition after irradiation.

References

1 He, Y., Hadar, I. & Kanatzidis, M. G. Detecting ionizing radiation using halide perovskite semiconductors processed through solution and alternative methods. *Nature Photonics* (2021).

2 Sedigh Rahimabadi, P., Khodaei, M. & Koswattage, K. R. Review on applications of synchrotron-based X-ray techniques in materials characterization. *X-Ray Spectrometry* **49**, 348-373 (2020).

3 Westneat, M. W., Socha, J. J. & Lee, W.-K. Advances in biological structure, function, and physiology using synchrotron X-ray imaging. *Annual Review of Physiology* **70**, 119-142 (2008).

4 Tang, F. *et al.* Synchrotron X-Ray Tomography for Rechargeable Battery Research: Fundamentals, Setups and Applications. *Small Methods* **5**, 2100557 (2021).

5 Willmott, P. *An introduction to synchrotron radiation: techniques and applications*. (John Wiley & Sons, 2019).

6 Prokesch, M., Soldner, S. A. & Sundaram, A. G. CdZnTe detectors for gamma spectroscopy and x-ray photon counting at 250 × 106 photons/(mm2 s). *J Appl Phys* **124**, 44503 (2018).

7 Spahn, M. X-ray detectors in medical imaging. *Nucl Instrum Meth A* **731**, 57-63 (2013).

8 Kasap, S. *et al.* Amorphous and polycrystalline photoconductors for direct conversion flat panel X-ray image sensors. *Sensors* **11**, 5112-5157 (2011).

9 Hatsui, T. & Graafsma, H. X-ray imaging detectors for synchrotron and XFEL sources. *IUCrJ* **2**, 371-383 (2015).

10 Bale, D. S. & Szeles, C. Nature of polarization in wide-bandgap semiconductor detectors under high-flux irradiation: Application to semi-insulatingCd1−xZnxTe. *Physical review. B, Condensed matter and materials physics* **77** (2008).

11 Bell, R. O., Entine, G. & Serreze, H. B. Time-dependent polarization of CdTe gamma-ray detectors. *Nuclear Instruments & Methods* **117**, 267-271 (1974).

12 Cola, A. & Farella, I. The polarization mechanism in CdTe Schottky detectors. *Appl Phys Lett* **94** (2009).

13 Abbene, L. *et al.* X-ray response of CdZnTe detectors grown by the vertical Bridgman technique: Energy, temperature and high flux effects. *Nucl Instrum Meth A* **835**, 1-12 (2016).

14 Veale, M. C. *et al.* Characterization of the uniformity of high-flux CdZnTe material. *Sensors* **20**, 2747 (2020).

15 Onodera, T., Hitomi, K. & Shoji, T. Spectroscopic performance and long-term stability of thallium bromide radiation detectors. *Nucl Instrum Meth A* **568**, 433-436 (2006).

16 Sato, G. *et al.* Study of polarization phenomena in Schottky CdTe diodes using infrared light illumination. *Nucl Instrum Meth A* **652**, 149-152 (2011).

17 Strassburg, M., Schroeter, C. & Hackenschmied, P. CdTe/CZT under high flux irradiation. *Journal of Instrumentation* **6**, C01055-C01055 (2011).

18 Gadkari, D. *et al.* Characterization of 128× 128 MM-PAD-2.1 ASIC: a fast framing hard x-ray detector with high dynamic range. *Journal of Instrumentation* **17**, P03003 (2022).

19 Tsigaridas, S. & Ponchut, C. X-ray imaging with high-Z sensors for the ESRF-EBS Upgrade. *Journal of Instrumentation* **14**, C04009 (2019).

20 Veale, M. C. *et al.* Cadmium zinc telluride pixel detectors for high-intensity x-ray imaging at free electron lasers. *Journal of Physics D: Applied Physics* **52**, 085106 (2018).

21 Buttacavoli, A. *et al.* Incomplete Charge Collection at Inter-Pixel Gap in Low-and High-Flux Cadmium Zinc Telluride Pixel Detectors. *Sensors* **22**, 1441 (2022).

22 Prokesch, M. *et al.* CdZnTe Detectors Operating at X-ray Fluxes of 100 Million photons /(mm^2sec). *IEEE Transactions on Nuclear Science* **63**, 1854-1859 (2016).

23 Bolotnikov, A. E. *et al.* Effects of Te Inclusions on the Performance of CdZnTe Radiation Detectors. *IEEE Transactions on Nuclear Science* **55**, 2757-2764 (2008).

24 Schieber, M. M. *et al.* Vol. 3768 296-309 (SPIE, 1999).

25 Scholz, J. *et al.* Biomedical x-ray imaging with a GaAs photon-counting detector: A comparative study. *APL Photonics* **5**, 106108-106108-106109 (2020).

26 Greiffenberg, D. *et al.* Characterization of GaAs: Cr sensors using the charge-integrating JUNGFRAU readout chip. *Journal of Instrumentation* **14**, P05020 (2019).

27 Wei, H. & Huang, J. Halide lead perovskites for ionizing radiation detection. *Nat Commun* **10**, 1066 (2019).

28 Cao, L. R., Pan, L., Kandlakunta, P. & Nie, W. in *Hard X-Ray, Gamma-Ray, and Neutron Detector Physics XXIII.* 118380B (International Society for Optics and Photonics).

29 Tsai, H. *et al.* Quasi-2D Perovskite Crystalline Layers for Printable Direct Conversion X-Ray Imaging. *Advanced Materials 34.13*, 2106498 (2022).

30 Kim, Y. C. *et al.* Printable organometallic perovskite enables large-area, low-dose X-ray imaging. *Nature* **550**, 87-91 (2017).

31 He, Y. *et al.* CsPbBr3 perovskite detectors with 1.4% energy resolution for high-energy γ-rays. *Nature Photonics* **15** (2020).

32 Pan, L., Feng, Y., Kandlakunta, P., Huang, J. & Cao, L. R. Performance of Perovskite CsPbBr3 Single Crystal Detector for Gamma-Ray Detection. *IEEE Transactions on Nuclear Science* **67**, 443-449 (2020).

33 Lei Pan, Y. H., Vladislav V. Klepov, Michael C. De Siena, and Mercouri G. Kanatzidis. Perovskite CsPbBr3 single crystal detector for high flux X-ray photon counting. *IEEE Transactions on Medical Imaging* (2022).

34 Kakavelakis, G. *et al.* Metal Halide Perovskites for High-Energy Radiation Detection. *Adv Sci (Weinh)* **7**, 2002098 (2020).

35 Yuan, Y. & Huang, J. Ion migration in organometal trihalide perovskite and its impact on photovoltaic efficiency and stability. *Accounts of Chemical Research* **49**, 286-293 (2016).

36 Lin, Y. *et al.* Suppressed ion migration in low-dimensional perovskites. *ACS Energy Letters* **2**, 1571-1572 (2017).

37 Wu, T., Ahmadi, M. & Hu, B. Giant current amplification induced by ion migration in perovskite single crystal photodetectors. *Journal of Materials Chemistry C* **6**, 8042-8050 (2018).

38 Baloch, A. A. *et al.* Analysis of photocarrier dynamics at interfaces in perovskite solar cells by time-resolved photoluminescence. *The Journal of Physical Chemistry C* **122**, 26805-26815 (2018).

39 Kirchartz, T., Márquez, J. A., Stolterfoht, M. & Unold, T. Photoluminescence‐based characterization of halide perovskites for photovoltaics. *Advanced Energy Materials* **10**, 1904134 (2020).

40 Jia, P. *et al.* The Trapped Charges at Grain Boundaries in Perovskite Solar Cells. *Advanced Functional Materials* **31**, 2107125 (2021).

41 Zeng, P., Feng, G., Cui, X. & Liu, M. Revealing the role of interfaces in photocarrier dynamics of perovskite films by alternating front/back side excitation time-resolved photoluminescence. *The Journal of Physical Chemistry C* **124**, 6290-6296 (2020).

42 Pan, L., Shrestha, S., Taylor, N., Nie, W. & Cao, L. R. Determination of X-ray detection limit and applications in perovskite X-ray detectors. *Nature Commun* **12**, 5258-5258 (2021).

43 Pan, L., Feng, Y., Huang, J. & Cao, L. R. Comparison of Zr, Bi, Ti, and Ga as Metal Contacts in Inorganic Perovskite $CsPbBr_3$ Gamma-Ray Detector. *IEEE Transactions on Nuclear Science* **67**, 2255-2262 (2020).

44 He, Y. *et al.* Sensitivity and Detection Limit of Spectroscopic-Grade Perovskite CsPbBr3 Crystal for Hard X-Ray Detection. *Advanced Functional Materials*, 2112925
45 He, Y. *et al.* Perovskite CsPbBr3 single crystal detector for alpha-particle spectroscopy. *Nucl Instrum Meth A* **922**, 217-221 (2019).
46 He, Y. *et al.* High spectral resolution of gamma-rays at room temperature by perovskite CsPbBr3 single crystals. *Nat Commun* **9**, 1609 (2018).
47 Toufanian, R., Swain, S., Becla, P., Datta, A. & Motakef, S. Cesium Lead Bromide Semiconductor Radiation Detectors: Crystal Growth, Detector Performance and Ionic Polarization. *Journal of Materials Chemistry C* (2022).
48 Olbinado, M. P. *et al.* MHz frame rate hard X-ray phase-contrast imaging using synchrotron radiation. *Optics Express* **25**, 13857-13871 (2017).
49 Ahmed, M. S., AL-Tulaihi, Y. & ALRikabi, H. Bandwidth Analysis of a p-π-n Si Photodetector. *International Journal of Computer Applications* **975**, 8887 (2016).
50 Dedic, V. *et al.* De-polarization of a CdZnTe radiation detector by pulsed infrared light. *Appl Phys Lett* **107** (2015).

Supplementary Files

This is a list of supplementary files associated with this preprint. Click to download.

- SICLBsynchrotron10162022.docx